Comparing VHF coherent scatter from the radar aurora with incoherent scatter and all-sky auroral imagery

D. Hysell,[1] R. Miceli,[1] J. Munk,[2] D. Hampton,[3] C. Heinselman,[4] M. Nicolls,[4] S. Powell,[5] K. Lynch,[6] and M. Lessard[7]

[1] VHF coherent scatter radar observations of an auroral substorm over Alaska are analyzed in the context of multibeam incoherent scatter plasma density and drifts data and green-line all-sky optical imagery. Coherent scatter arises from Farley Buneman waves which are excited in the E region whenever the convection electric field is greater than about 20 mV/m. Aperture synthesis radar imaging and other aspects of the methodology facilitate the precise spatial registration of the coherent scatter with coincident optical and incoherent scatter radar measurements. Discrete auroral arcs were found to separate diffuse regions of coherent backscatter and, sometimes, to align with the boundaries of those regions. At other times, auroral arcs and torches lined up adjacent to discrete, structured regions or radar backscatter. Drastic variations in the Doppler shifts of the coherent scatter from one side of the auroral forms to the other suggest the presence of field-aligned currents. An empirical formula based on previous studies but adapted to account approximately for the effects of wave turning was used to estimate the convection electric field from the moments of the coherent scatter Doppler spectra. Line-of-sight F region plasma drift measurements from the Poker Flat Incoherent Scatter Radar (PFISR) were found to be in reasonable agreement with these convection field estimates. Reasons why the empirical formulas may be expected to hold are discussed.

1. Introduction

[2] The auroral E region ionosphere is coupled by magnetic field lines to the magnetosphere which imposes energetic particle precipitation and electromagnetic and electrostatic fields. Ionospheric heating results from precipitation and from the Pedersen and parallel currents driven by the convection field (Joule heating). At the same time, the Hall currents that arise drive modified two-stream (also called "Farley Buneman") instabilities [*Farley*, 1963; *Buneman*, 1963] and generate a spectrum of field-aligned ionospheric irregularities (FAIs). Farley Buneman waves can modify the mean state of the ionosphere through wave heating [*Schlegel and St.-Maurice*, 1981; *St.-Maurice et al.*, 1981; *St.-Maurice and Laher*, 1985; *St.-Maurice*, 1990; *Milikh and Dimant*, 2002, 2003; *Bahcivan*, 2007]. Electron and ion thermal instabilities may also contribute additional heating at the altitude extremes of the E region [*Kagan and Kelley*, 2000; *St.-Maurice and Kissack*, 2000; *Dimant and Oppenheim*, 2004; *Oppenheim and Dimant*, 2004].

[3] Farley Buneman waves and turbulence modify the temperature and therefore the chemistry, conductivity, and transport locally. By modifying chemical rate constants, they can alter the plasma density, composition, and conductivity. Heating also modifies the neutral circulation which, coupled with changes in ion drag and with Lorentz forcing, can contribute to neutral wind surges, gravity waves, traveling atmospheric disturbances, and traveling ionospheric disturbances that propagate away from their point of origin and ultimately affect ionospheric stability at lower latitudes [*Fuller-Rowell et al.*, 1994].

[4] Coherent radar backscatter from auroral E region FAIs can be measured with great precision and accuracy compared to many other ground-based ionospheric diagnostics. But what do the echoes tell us about the ionospheric state variables and the convection and heating in particular?

[1] Earth and Atmospheric Sciences, Cornell University, Ithaca, New York, USA.

[2] Electrical Engineering, University of Alaska Anchorage, Anchorage, Alaska, USA.

[3] Geophysical Institute, University of Alaska Fairbanks, Fairbanks, Alaska, USA.

[4] SRI International, Menlo Park, California, USA.

[5] Electrical and Computer Engineering, Cornell University, Ithaca, New York, USA.

[6] Physics and Astronomy, Dartmouth College, Hanover, New Hampshire, USA.

[7] Institute for the Study of Earth, Oceans, and Space, University of New Hampshire, Durham, New Hampshire, USA.

Corresponding author: D. Hysell, Earth and Atmospheric Sciences, Cornell University, Ithaca, NY 14853, USA. (dlh37@cornell.edu)

Linear, local Farley Buneman wave theory offers only one reliable prediction — that the irregularities form only when and where the relative electron-ion drift speed exceeds the local ion acoustic speed. Different ansatz and heuristic theories, quasilinear, anomalous, and nonlocal analytic theories make different predictions about the Doppler spectra, with varying degrees of experimental support (see *Hamza and St-Maurice* [1993] and *Bahcivan et al.* [2005] for reviews.)

[5] The most complete contemporary theory is represented by the particle-in-cell simulations presented by *Oppenheim et al.* [2008] and *Dimant and Oppenheim* [2008]. Their two- and three-dimensional, fully kinetic and nonlinear simulations predict that the Doppler shifts of coherent scatter from Farley Buneman waves should be given approximately by the product of the ion acoustic speed and the cosine of the flow angle (the angle between the convection velocity and the line of sight). The Doppler width is predicted approximately by the product of the sine of the flow angle and a fraction (about one half) of the ion acoustic speed. Due to thermal effects, the simulated waves actually propagate at an angle slightly offset from the electron convection, and so the sine and cosine dependencies apply to an angle slightly offset from the flow angle [*Oppenheim and Dimant*, 2004]. The ion acoustic speed itself increased with the convection electric field through wave heating, making the Doppler spectra indirect indicators of the convection speed and direction.

[6] Testing the aforementioned predictions experimentally is challenging, in part because of the difficulty in estimating the ion acoustic speed (C_s) at E region altitudes. Note that C_s varies with the electron and ion temperatures and with the ratios of specific heat, themselves functions of the Farley-Buneman wave frequency, wave number, altitude, and other parameters. The experimental picture is consequently complicated and most likely looks different to different instruments. *Makarevich* [2009] summarized the published experimental findings pertaining to the Doppler spectra of the radar aurora. Most of the data were obtained using the 140 MHz STARE radar in Scandinavia or with high-latitude SuperDARN stations. While the review found that the $C_s \cos \theta$ prediction is realized in some cases at small flow angles, the experimental database is inconsistent and varies from instrument to instrument. *Makarevich* [2009] interpreted the experimental record in terms of linear theory and the possible effects of oblique (i.e. non perpendicular to B) radar ray paths but arrived at no simple, universal laws.

[7] Nevertheless, the experimental picture is not inconclusive. In the equatorial electrojet, the electron convection is generally rapid enough to excite Farley Buneman waves around midday but seldom strong enough to cause significant wave heating. During counter electrojet conditions, Farley Buneman waves can be excited when gradient drift waves are absent, greatly simplifying interpretation. By utilizing the simple scattering geometry at the magnetic equator and the simple relationship between slant range and flow angle, it can readily been seen that the Doppler shifts and spectral widths of VHF echoes from Farley Buneman waves during counter electrojet conditions vary as the cosine and sine, respectively, of an angle offset from the flow angle by about 10 degrees [*Woodman and Chau*, 2002; *Hysell et al.*, 2012].

[8] Using a small VHF coherent scatter radar imager located in Anchorage, Alaska, *Bahcivan et al.* [2005] and *Hysell et al.* [2008, 2009] observed Farley Buneman wave Doppler spectra that were also broadly consistent with the simulation results of *Oppenheim et al.* [2008]. They found that the Doppler shifts and spectral widths of the echoes were approximately proportional to the cosine and sine of the flow angle, respectively, multiplied by a monotonically increasing function of the convection speed that they interpreted as representing the ion acoustic speed. These results were obtained with minimal ambiguity through comparisons with electric field measurements from sounding rockets and from the Poker Flat Incoherent Scatter Radar (PFISR) in common volumes. The comparisons yielded empirical formulas which showed promise as tools for inferring the convection electric field from E region backscatter with very fine spatial and temporal resolution (when Farley Buneman waves are present and when the radar echoes are not attenuated by absorption). The specific formulas were adapted from those proposed by *Nielsen and Schlegel* [1983, 1985].

[9] In 2011, a modernized VHF coherent scatter radar imager was deployed in Homer, Alaska for observing the "radar aurora," the coherent scatter radar manifestation of the aurora, in the vicinity of the Poker Flat Rocket Range and the volume over it probed by the PFISR radar. Observations were made throughout the winter of 2012 with the 30 MHz radar, the PFISR, and with extensive support from optical instrumentation in Alaska. In this paper, we continue the investigation of the relationship between coherent scatter Doppler spectra from Farley Buneman waves and the background convection electric field and other ionospheric parameters. Comparisons with data acquired by the MICA sounding rocket, which was launched on February 19, 2012, in the middle of our study, will be presented in subsequent papers.

2. Data Presentation

[10] A 30 MHz software-defined coherent scatter radar imager has been deployed on Diamond Ridge overlooking Homer, Alaska, for observing the radio aurora. Viewed from Homer, the locus of perpendicularity at E-region altitudes extends from about 64–68 degrees latitude and encompasses most of the Poker Flat Rocket Range (see Figure 1) [see also *Tsunoda et al.*, 1974]. The main beam of the radar can be steered in the direction of Poker Flat, making common-volume observations with the PFISR possible. The radar uses six coplanar antenna arrays for reception, giving fifteen independent interferometry baselines, the longest of which being 15 wavelengths long in the magnetic east–west direction. Aperture synthesis radar imaging is employed to estimate the distribution of the received power in azimuth and elevation angle as well as Doppler frequency and time (see *Hysell and Chau* [2006] for a discussion of the methodology). This is a super-resolution technique with an azimuth angle resolution as fine as about 0.5 degrees in practice for high signal-to-noise ratio (SNR) targets. The range resolution of the radar, which employed a 13-bit Barker code, was 2.25 km during the experiments discussed here, and the interpulse period was 4 ms, so that Doppler velocities between ± 625 m/s could be detected without frequency aliasing. A typical incoherent integration time for Homer radar data is 5 s. The half-power full beamwidth of the Homer radar transmission pattern, which is directed toward magnetic north and toward Poker Flat, is approximately $10°$. The
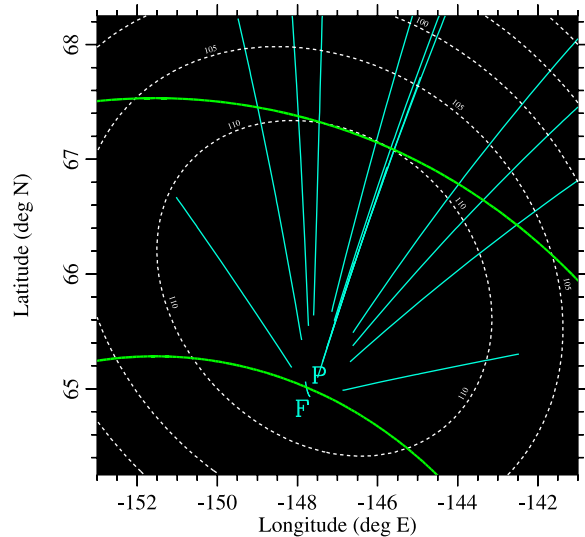
Figure 1. Plan view of the auroral observations. Cyan lines denote the 15 PFISR radar beams, mapped downward along magnetic field lines to an altitude of 110 km. The green lines bound the radar ranges sampled by the coherent scatter radar in Homer. The white contours indicate the altitudes where the condition for field-aligned backscatter is satisfied from Homer, neglecting the effects of refraction. The "P" and "F" symbols denote the locations of Poker Flat and Fairbanks, respectively.

beamwidth between first nulls is approximately twice as wide.

[11] For our experiments, the PFISR radar cycled between 15 pointing positions on a pulse-to-pulse rotation. Both long pulses and randomized alternating coded pulses were used. Parameters were estimated using a combination of conventional gated analysis and model-based inference, as will be described below.

[12] Figure 2 summarizes the auroral activity on February 19, 2012. Figure 2a shows estimates of the convection derived from line-of-sight incoherent scatter long-pulse drifts measurements. For these measurements, the PFISR cycled between 15 different pointing positions, 6 of which being in the plane of the magnetic meridian. Vector convection at different magnetic latitudes was estimated from the data using a regularization procedure which assumes the convection to be invariant with magnetic longitude [*Heinselman and Nicolls*, 2008]. According to the figure, convection was strong and westward throughout most of the evening, becoming slow and southward around 0600 UT and turning eastward (red arrows) briefly around 0700 UT.

[13] Figure 2b shows plasma number density estimates derived from power measurements from a single PFISR beam in the magnetic meridian with a 38° elevation angle. These data derive from an alternating code experiment. Corrections for the electron ion-temperature ratio have not been applied to these estimates. (The corrections would improve accuracy at the cost of precision.) The data indicate modest, periodic (half-hourly) enhancements in *E*-region ionization between 0440–0610 UT. The density enhancements after 0530 UT penetrated into the *D* region, creating the conditions for significant absorption of the low-elevation
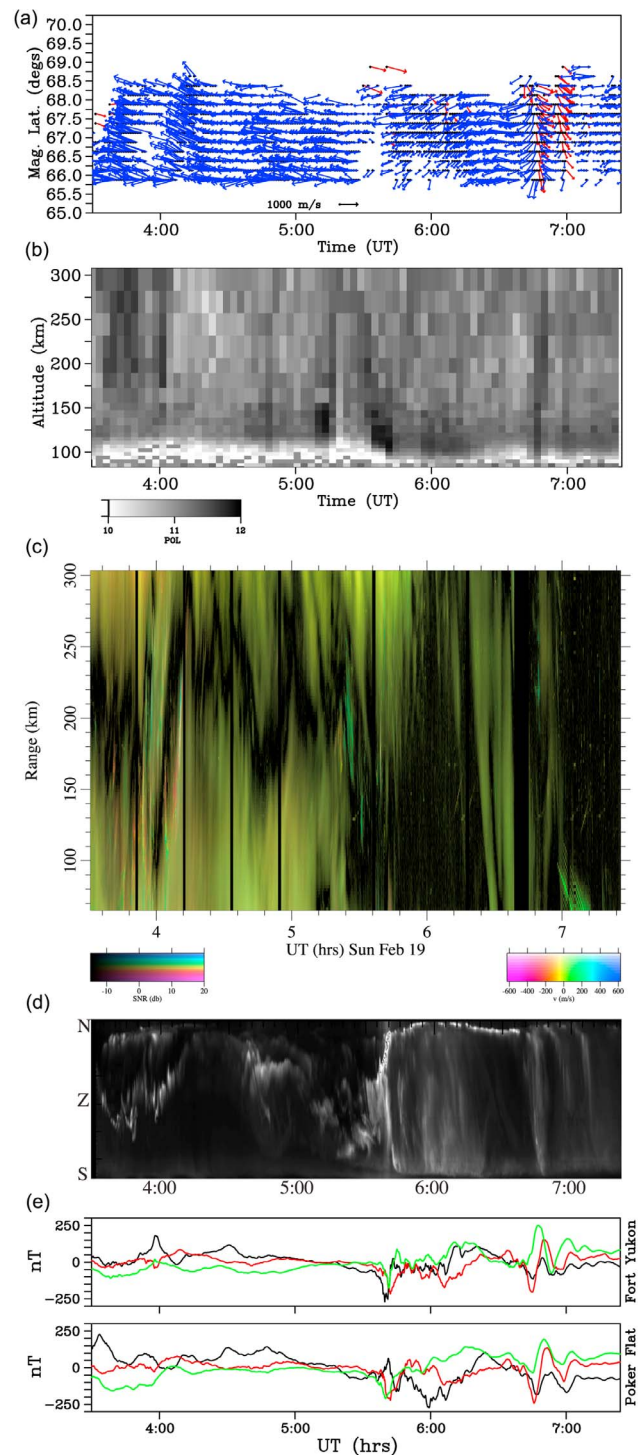
Figure 2. Auroral observations made on February 19, 2012. (a) Horizontal plasma convection estimated from PFISR line-of-sight incoherent scatter drifts measurements. (b) Uncorrected plasma number density estimates from a single PFISR pointing position. (c) Coherent backscatter recorded by the Homer radar imager (see text). (d) 557.7 nm emissions from the Poker Flat Meridian Scanning Photometer (MSP) from (N) north to (S) south. (e) Data from the Poker Flat and Fort Yukon magnetometers. The black, red, and greed lines signify the H, D, and Z magnetic field components, respectively.
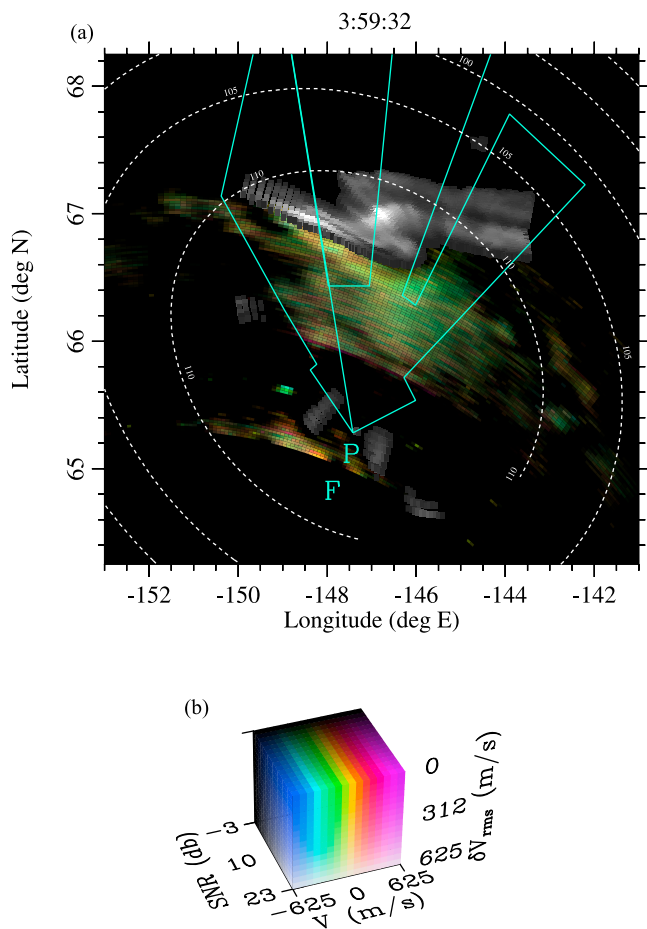
Figure 3. Representative radar imagery from 0359 UT during the Feb. 19, 2012 auroral event. Radar data are represented by colored pixels according to the scale shown and described earlier in the text. Optical imagery from the Fort Yukon all-sky imager is superimposed in gray shades. White contours show the altitude where rays from the Homer radar are perpendicular to the geomagnetic field, neglecting the effects of refraction. Cyan lines outline the rocket launch zones from the Poker Flat Rocket range.

radar signals from Homer. Enhancements in the F-region density occur where the convection undergoes rapid changes.

[14] Figure 2c shows coherent backscatter data from the Homer radar in range-time-Doppler-intensity (RTDI) format. Here, range is apparent slant range. True slant range from Homer to the E-region scatterers is calculated by adding 600 km to this figure. For comparison with the ISR data, the ranges shown span magnetic latitudes from about 65–67 degrees. This mapping is imprecise due to the wide field of view of the Homer radar (recall Figure 1).

[15] The pixels in the RTDI plot convey information about the Doppler spectrum, with the brightness, hue, and saturation signifying the SNR (−13–20 dB), the Doppler shift (±625 m/s), and the spectral width (0–625 m/s). Red (blue) hues are redshifted (blueshifted). Pure (pastel) colors are spectrally narrow (wide). The pastel, yellowish tones that dominate the figure signify broad spectra with small red

shifts. Purer tones centered around 0400 UT and 0540 UT signify narrow Doppler spectra with large red and blue shifts. The near cessation of echoes around 0600 UT was likely associated with absorption. Note that even the specular meteor echoes clearly visible after 0700 UT are invisible around 0600 UT. An interesting feature of this dataset is a persistent absence of echoes at intermediate ranges, with the exception of the period around 0630 UT when all the range gates contained echoes.

[16] Figure 2d represents optical emissions from the 557.7 nm channel of the Poker Flat Meridian Scanning Photometer (MSP). A substorm is clearly underway around 0540 UT, explaining the electron precipitation and the radio absorption. Optical enhancements throughout the evening are obviously correlated with density enhancements in Figure 2b above. Meridional excursions in the locations of the brightest optical emissions are meanwhile reminiscent of the range excursions in the coherent scatter returns in Figure 2c. Below, we will show how auroral arcs generally fall in the gaps between regions of diffuse coherent scatter. The exclusivity of optical emissions and coherent scatter will be more obvious in imaging analyses.

[17] Finally, magnetometer traces from Poker Flat and Fort Yukon are shown in Figure 2e. The relatively large H components (>100 nT) prior to 0500 UT are consistent with the periods of rapid convection in the PFISR data, and the deflections in the D component around 0700 UT are coincident with the convection reversal. The largest variations in the H component around 0600 occurred during the D region precipitation/absorption interval.

[18] Neutral winds were measured during the event by imaging Fabry Perot interferometers (FPI) observing red- and green-line emissions (M. Conde, personal communication, 2012). The FPI data indicate steady neutral flows in the magnetic westward direction in the E and F regions throughout the entire auroral event described here.

2.1. Comparison With Optical Imagery

[19] Figure 3 shows a combination of radar imagery from the Homer radar and superimposed optical imagery from the Fort Yukon all-sky imager for a representative snapshot of the auroral event. The radar imagery was derived using aperture synthesis imaging methodology. Note that the radiation pattern of the Homer radar antennas used for transmission restricts echoes to azimuths close to the magnetic meridian. Range gating further restricted the latitudes sampled to between about 65–67 degrees.

[20] While the radar imagery is three dimensional and contains information about the altitude of the scatterers, that information is not very accurate, and a scattering altitude of 110 km is assumed to simplify the graphical projection of the radar data onto geographic coordinates. Similarly, the green-line optical imagery from Fort Yukon is also projected assuming a 110-km altitude emission height. The cadence of the optical imagery was resampled at 5-s intervals to match the radar data stream.

[21] Additional imagery for selected times during the auroral event is shown in Figure 4. A common feature of datasets like these is the near mutual exclusion of radar echoes and optical emissions. At 0330 UT, the ranges unoccupied by radar echoes are seen to be occupied by a discrete auroral arc. By 0336, the arc had moved northward
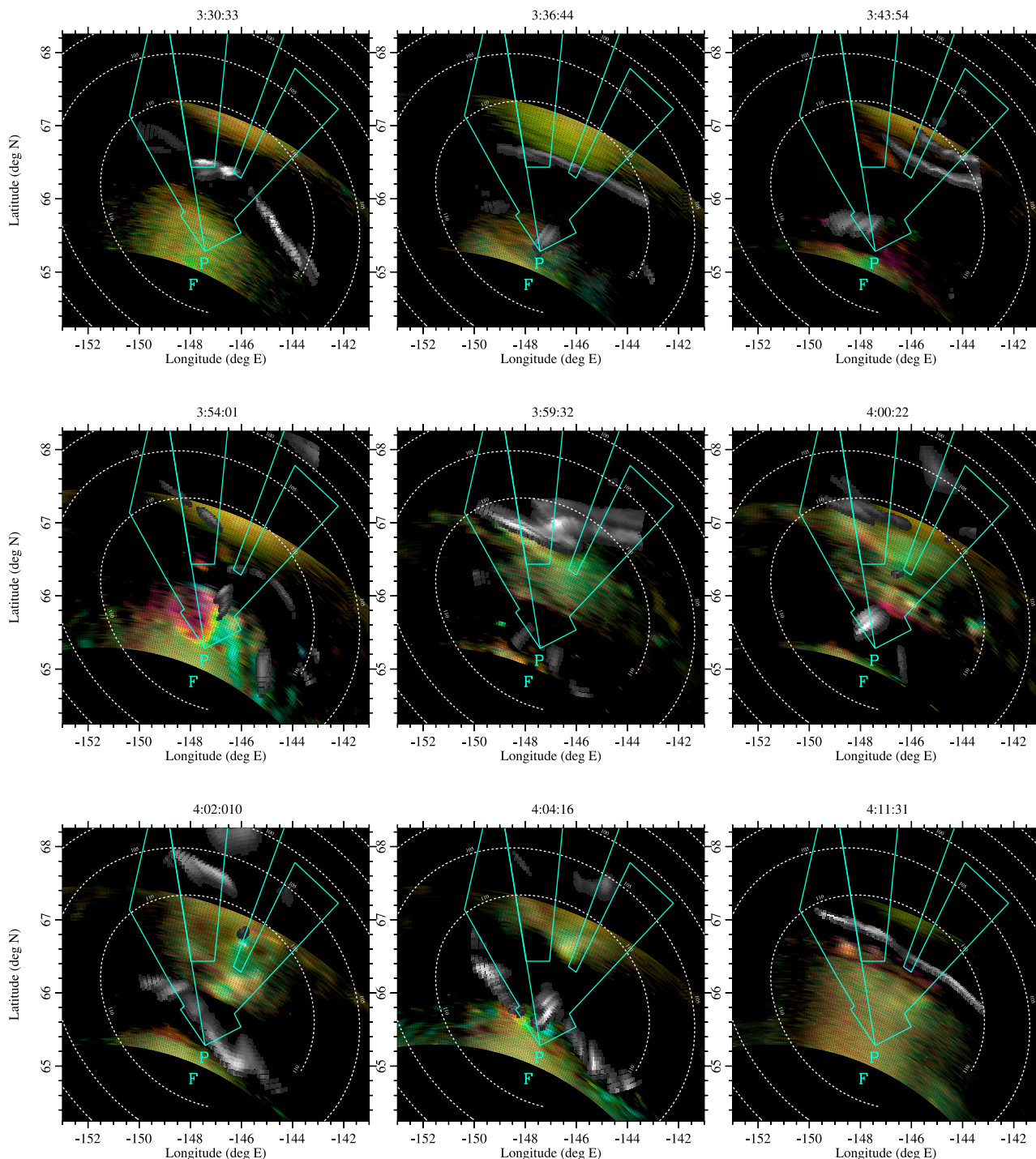
Figure 4. Additional radar imagery at selected times during the Feb. 19, 2012 auroral event.

to define the lower edge of the radar scattering region. Some auroral torches had appeared by this time at lower latitudes which separated scattering regions with relatively large and small Doppler shifts to the west and the east of Poker Flat, respectively. Throughout the remainder of the images, torch-like auroral forms can be seen delineating structured coherent backscatter at low latitudes while discrete arcs at higher latitudes either bounded the regions of coherent scatter or occupied regions from which no radar scatter was detected.

[22] The characteristics of VHF coherent scatter and the radar aurora in comparison to the more familiar optical aurora were reviewed recently by *Bahcivan et al.* [2006]. The two phenomena have been found to be closely associated, and investigators consider "diffuse" and "discrete" radar aurora in analogy to the optical terminology and the tendency for echoes to arise from either broad or narrow spans of ranges in radar RTI diagrams, respectively [e.g., *Greenwald et al.*, 1973; *Tsunoda et al.*, 1976; *Providakes*
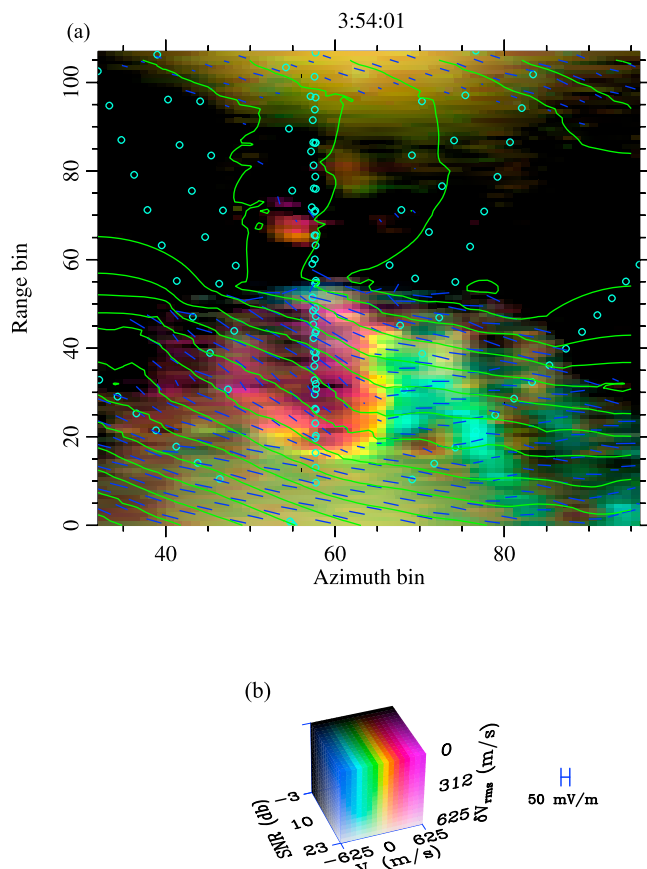
Figure 5. Figure illustrating how coherent and incoherent scatter radar data can be compared. The horizontal and vertical axes span the azimuth and range bins of the coherent scatter radar data. The first three moments of the coherent scatter Doppler spectra (SNR, Doppler shift, and spectral width) are represented by the pixel coloring. Cyan circles represent the sampling of the PFISR long-pulse line-of-sight drifts measurements, mapped to an altitude of 110 km along magnetic field lines. Blue linesegments are estimates of the convection speed (see scale below). Green contours are an estimated convection pattern, with contours plotted at 1 kV intervals (see text).

et al. 1985]. Most often, the diffuse radar aurora has been seen equatorward of auroral arcs while discrete radar aurora is seen poleward of them. Discrete radar aurora is also often concentrated immediately adjacent to auroral arcs and is thought to be associated with strong polarization electric fields that form at their boundaries. Polarization is inevitable in view of the attendant, sharp conductivity gradients across auroral arcs and the strong background convection. This is in contrast to the diffuse radar aurora, which can be produced by strong, uniform convection in the absence of auroral arcs entirely. The high conductivity within the arcs, meanwhile, is thought to suppress electric fields locally and to inhibit Farley Buneman instability, leading to an absence of echoes from within arcs. Strong waves can however form in the adjacent return current regions (i.e. in black aurora).

[23] Finally, *Bahcivan et al.* [2006] pointed out that the reversal of the Doppler shifts of radar echoes from one side of an auroral arc to the other may be evidence of field-aligned currents (FAC) whereas polarization in the absence of FAC should produce echoes with similar Doppler shifts on either side of an arc. The argument is that the transverse electric fields accompanying FAC are monopolar and have odd symmetry about an irregularity whereas the dielectric response of an irregular plasma to background electric fields is dipolar with even symmetry. This remains true in anisotropic plasmas [*Hysell and Drexler*, 2006]. This reasoning is sound but somewhat oversimplified, neglecting possible effects of sharp gradients in the convection electric field, the temperature, or the radio absorption, for example. Nevertheless, the symmetry of the Doppler shifts of scatter surrounding an arc can be suggestive of the presence of field-aligned current.

[24] The features in Figure 4 are mostly consistent with the scenarios described above except for the occurrence of diffuse radar aurora both equatorward and poleward of an auroral arc at times and the presence of structured backscatter (in terms of SNR and Doppler shifts) in the absence of discrete auroral forms. That the Doppler shifts of the echoes are highly structured in space near the auroral torches suggests that strong FACs are present in those auroral features.

2.2. Comparison With Incoherent Scatter Drifts

[25] Here, we establish a framework for comparing the coherent scatter imagery with the incoherent scatter line-of-sight drifts measurements and for interpreting the Doppler spectra of the radar aurora in terms of the convection electric field. The comparison of the radar datasets is most easily carried out in the native reference frame of the coherent scatter radar data, which is illustrated in Figure 5. This figure shows the same snapshot as one of the frames in Figure 4 (0354 UT). This time, however, the abscissa and ordinate for the plot are the azimuth angle and range bin, respectively, for the imaging data. Range bins number from 0 to 106 and denote relative range increments of 2.25 km, starting from a range offset of 660 km. Azimuth bins number from 0 to 127 and denote azimuth direction cosines uniformly sampled between ±0.4, with a direction cosine of zero indicating an azimuth parallel to the magnetic meridian and in the approximate direction from Homer to Poker Flat. In fact, only azimuth bins from 31–95 (direction cosines between ±0.2) are included in the plot, since the main transmitting antenna beams fall entirely within this span.

[26] The pixel colors once again convey information about the first three moments (SNR, Doppler shift, spectral width) of the underlying coherent scatter Doppler spectra. This particular data interval was selected for its spectral diversity from range to range, azimuth to azimuth. The cyan circles, meanwhile, represent the sampling scheme of the PFISR long-pulse incoherent scatter drifts measurements. The physical centers of 255 ISR scattering volumes (15 beams times 17 range gates) were mapped along magnetic field lines to an altitude of 110 km and plotted as circles here. As 6 of the PFISR beams are in the magnetic meridian plane, a disproportionate number of the plotted points fall nearly along a line parallel to the magnetic meridian.

[27] We regard the PFISR *F* region drifts as the projections of the plasma $\mathbf{E} \times \mathbf{B}$ drift velocity along the given radar line of sight. Knowledge of the transverse vector electric field across the plane represented by Figure 5, a plane essentially perpendicular to the geomagnetic field, would be sufficient

information for predicting the incoherent scatter drifts measurements. We can attempt to infer the transverse electric field wherever coherent scatter data are available from the Doppler shift and spectral width of the echoes in the given range and azimuth angle bin. This can be done using empirical formulas similar to those found in earlier studies of the radar aurora, viz.

$$\langle \omega/k \rangle = V_\circ \cos(\theta - \theta_\circ) + v_i \tag{1}$$

$$\langle \delta\omega/k \rangle_{\mathrm{rms}} = \frac{1}{2} V_\circ |\sin(\theta - \theta_\circ)| \tag{2}$$

$$V_\circ = 350 + (V_d/100)^2 \tag{3}$$

(SI units) where $\langle \omega/k \rangle$ is the Doppler shift, $\langle \delta\omega/k \rangle_{\mathrm{rms}}$ is the spectral width, v_i is the line-of-sight E-region, wind-induced ion drift speed, and $V_\circ$ is an auxiliary variable related quadratically to the electron convection speed V_d and presumed to be associated with the ion acoustic speed. Also, θ is the flow angle with respect to the radar line of sight and $\theta_\circ$ is an offset representing turning due to thermal effects. (Note that wave turning has not been considered previously in similar analyses.) For this study, we take $\theta_\circ = 10°$ and $v_i = 0$ in view of the fact that the neutral winds are thought to be mainly transverse to the radar lines of sight.

[28] The empirical model equations can be inverted in every bin of the radar image to find the convection speed and direction from the coherent scatter spectral moments provided that the echoes are strong enough for high-quality moment estimation and with the assumption that the convection is strictly westward (right-to-left) or eastward (left-to-right) from the radar perspective.

[29] Performing the inversion under the assumption of westward convection leads to the blue line segments in Figure 5, estimates of the electron convection speed and direction. (Note that only a very small fraction of the estimates available are actually drawn here to avoid an overly cluttered figure.) The convection is predicted here to be faster at low latitudes than at high latitudes and to have significant northern (southern) components looking magnetic east (west). The estimates generally vary gradually in space. The empirical model does not admit solutions for the convection speed less than 350 m/s or about 17.5 mV/m. We assume the convection speed is less than this in regions free of coherent scatter, although absorption could also be at work.

[30] Given a number of pointwise estimates of the electron convection speed and direction, it is possible to construct a complete convection pattern from the coherent scatter radar data. The pattern can later be compared with PFISR line-of-sight drifts measurements for validation. The problem is mixed-determined and possibly poorly conditioned, but these issues can be addressed by using a least squares solver for the potential field augmented with a suitable regularization scheme [e.g., *Aster et al.*, 2005]. Here, we solve numerically for a potential field by globally penalizing 1) inconsistency with the radar-derived convection velocity estimates and also 2) nonuniformity. An adjustable regularization parameter weights the penalties.

[31] Equipotential contours found through the regularization procedure described above are shown superimposed on Figure 5 in green. The contours are spaced at 1 kV intervals. The contours serve as streamlines of the flow, and their separation is indicative of the strength of the convection electric field. The contours thus found are consistent with the individual convection velocity estimators, as they must be, while being as smooth as the data permit. In regions where no data are available, the potential solution relaxes to a uniform solution. While we do not expect the solution to be very accurate where there are no data, we can at least infer that the convection is not very rapid there from the very absence of Farley Buneman waves.

[32] We would not expect a set of velocity estimates to conform to a potential flow field in general unless they accurately portray an incompressible flow. A metric for validating the convection velocity estimates derived from the radar aurora is the residual obtained in computing the electrostatic potential function in Figure 5. For this example, the RMS discrepancy in the velocity estimates from the model convection pattern as a fraction of the total model RMS electric field is less than 20%. This is a modest figure which could be reduced further with a reduction of the regularization parameter enforcing the smoothness of the solution (with a reduction of the stability of the algorithm).

[33] Validating the convection pattern estimates obtained from coherent scatter is essential. *Bahcivan et al.* [2006] and *Hysell et al.* [2008, 2009] validated against in situ electric field measurements from the JOULE and JOULE II sounding rockets. In this study, we attempt to validate against the PFISR F region line-of-sight ion drift measurements. Note that we cannot compare our results with the convection estimates in Figure 2a, since those were obtained with the assumption of L-shell invariance. This assumption is permissible for estimating large-scale circulation but obviously neglects the fine structure within the volume illuminated by the coherent scatter radar that we are attempting to recover.

[34] The strategy will be to use whatever coherent scatter data are available in the vicinity of the cyan circles in Figure 5 to predict the convection there and, subsequently, the line-of-sight F region ion drifts observed by the PFISR, assuming equipotential field lines and perfect mapping into the F region. Another implicit assumption is that the field-aligned F region ion drifts are negligible.

[35] Figure 6 is a scatterplot comparing measured PFISR line-of-sight drifts (horizontal axis) with drifts predicted from the corresponding coherent scatter Doppler spectra from essentially common field lines (vertical axis). In constructing this figure, only PFISR drift data with relative RMS errors less than 12.5% were used, and only coherent scatter data from bins with SNR > 6 dB were considered. The PFISR data were integrated for 1 min. for satisfactory statistical confidence, whereas the coherent scatter data cadence was once every 5 s. Rather than averaging the latter down to a 1 min. cadence, we simply plot points for all data conjunctions, meaning that up to 12 points may be plotted for each single PFISR measurement. Plotting colors are changed cyclically each minute to help highlight the 12-point clusters. This illustrates the temporal variability in the coherent scatter data. One minute is a long time insofar as auroral phenomenology is concerned.

[36] The plotted points in Figure 6 fall mainly into three "islands" representing the westward-, northward-, and eastward-pointing PFISR beams, respectively. A more varied
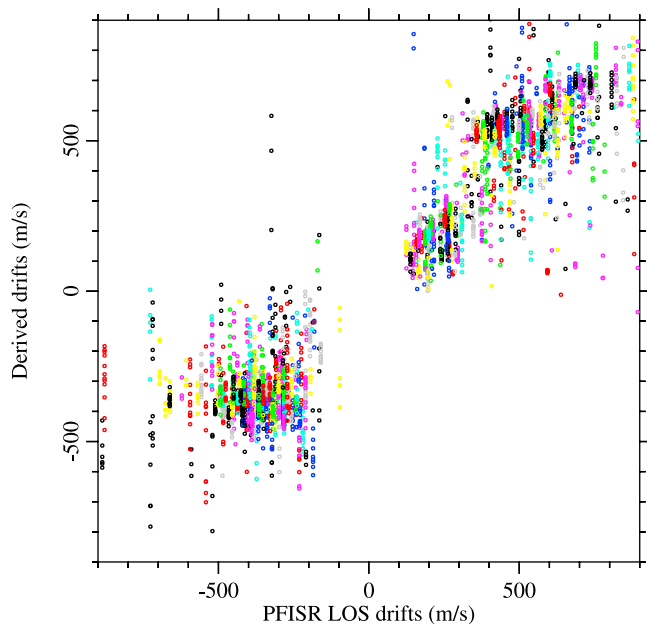
Figure 6. Measured PFISR line-of-sight drifts (horizontal axis) versus predictions on the basis of coherent scatter Doppler spectra (vertical axis). Data from 0330 – 0700 UT entered into the analysis.

distribution of pointing positions would help to populate the main diagonal more uniformly. Nevertheless, there is enough variability in the measurements to draw conclusions about the correspondence.

[37] Overall, Figure 6 shows that the data conjunctions mainly fall close to the main diagonal. The correlation coefficient for Figure 6 is 0.90. While scatter is present, this is exaggerated by the fact that the plotted points near the main diagonal overplot and conceal more points beneath. Possible sources of scatter are numerous. The RMS errors in the incoherent scatter data are necessarily significant. Spatial collocation in our comparison scheme is imperfect, and temporal coincidence is poor, as described above. The comparison breaks down in the event of spectral aliasing in the coherent scatter data or of eastward flows anywhere in the radar-illuminated volume. It breaks down where the line-of-sight *E*-region neutral winds are significant. Meteor echoes and other clutter in the VHF radar data contaminate the analysis. Furthermore, we have assumed no parallel ion drifts, although such drifts are certainly expected where auroral heating is occurring.

[38] An additional source of discrepancy is the spatial ambiguity associated with the ISR measurements. The PFISR used a ~72 km long pulse for the *F*-region measurements which was oversampled in range such that the samples overlapped significantly. This spatial low-pass filtering compounds the filtering implied by temporal integration. Spatial filtering also arises from the imperfect mapping of electric fields from *E*- to *F*-region altitudes due finite parallel conductivity [*Farley*, 1959]. This preferentially maps large scale electric field features while attenuating small-scale features.

[39] Nonetheless, the correspondence between the measured and the predicted drifts is rather good, suggesting that

coherent scatter from the radar aurora can be a reliable, quantitative tracer of ionospheric convection at high latitudes. The reasons for this empirical finding are not entirely clear, however. Some of the key ideas for understanding the association are described below. Before concluding the data presentation section, however, it should be emphasized that our ability to associate coherent scatter Doppler shifts with plasma convection relies on precise spatial collocation and radar imaging. The absence of obvious correlation between the incoherent scatter vector drifts estimates in Figure 2 and the coherent scatter Doppler shifts represented below them (and computed without radar imaging) illustrates how coarse spatial averaging destroys the association.

3. Discussion

[40] Auroral heating by Farley Buneman waves is often overlooked in theoretical studies and model calculations of the auroral energy budget and associated phenomena, including neutral forcing and auroral ion outflow. The heating can be highly intermittent in space and time, and no generally accepted parametrization of the process exists. Incoherent scatter radars can detect both the strong convection that drives the instabilities and the resulting *E* region heating, but only with relatively coarse spatial and temporal resolution and only when and where the ISR is operating. Monitoring the intense coherent radar backscatter from auroral *E* region FAIs offers a means of diagnosing Farley Buneman waves regionally with fine spatial and temporal resolution. But how should coherent scatter Doppler spectra be interpreted, and what do they convey about the waves and wave heating?

[41] A useful reference model for interpreting Farley Buneman wave heating was suggested by *Milikh and Dimant* [2002] which rests upon the following assumptions:

[42] 1. The RMS transverse electric field for Farley Buneman waves is equal to the background convection electric field.

[43] 2. The magnetic aspect angle of Farley Buneman waves, $k_\parallel/k_\perp$, is as large as is necessary to maintain the condition for marginal growth, i.e. a linear growth rate near zero.

[44] Here, $k_\parallel$ and $k_\perp$ refer to the wave number components parallel and perpendicular to the geomagnetic field, respectively. The model can be extended to apply to a stochastic spectrum of waves, with $k_\parallel/k_\perp$ replaced by $\langle k_\parallel/k_\perp \rangle_{\mathrm{RMS}}$ in that case. *Milikh and Dimant* [2002] were able to use this model to predict electron temperature enhancements observed by incoherent scatter radars as a function of the background convection electric field. The heating predicted by their model was associated entirely with the parallel wave number components of the Farley Buneman waves. Insofar as a prediction for coherent scatter from Farley Buneman waves goes, the marginal growth assumption suggests that coherent scatter Doppler shifts should be bounded by the ion acoustic speed in the scattering volume.

[45] Building on theoretical work by *Hamza and St-Maurice* [1993], *Hysell et al.* [2008] extended Milikh and Dimant's model, including effects of secondary Farley Buneman waves excited by the perturbation electric fields of the primary waves. *Hysell et al.* [2008] assumed that primary and secondary waves alike obey the condition for marginal linear stability. They

further assumed that the plasma density gradients due to the former were available to modify the linear growth rate of the latter. Assuming further that coherent radar backscatter at VHF frequencies is due mainly to scattering from the secondaries, *Hysell et al.* [2008] argued that the observed radar Doppler shifts should be proportional to the ion acoustic speed times the cosine of the flow angle and that the spectral width should be proportional to the ion acoustic speed times the sine of the flow angle times a parameter less than unity.

[46] Wave propagation at angles slightly offset from the electron convection can be understood in terms of ion thermal effects [*Oppenheim and Dimant*, 2004; *Dimant and Oppenheim*, 2004]. The perturbation electric fields of the Farley Buneman waves heat (frictionally) electrons and ions differentially in different phases of the waves. Moreover both species, but particularly the electrons, also undergo adiabatic heating (cooling) in wave-driven density enhancements (rarefactions). Electron temperature perturbations across individual waves, resulting mainly from thermodynamic effects, are nearly in phase with the original density perturbations. Ion temperature perturbations, resulting mainly from wave heating, are meanwhile out of phase with the original density perturbations, with temperatures elevated in regions of depleted density. The ion heating therefore causes pressure increases in the already depleted regions, leading to further depletion and wave growth. The mechanism is most effective for propagation directions offset from the main convection. The mechanism reduces the E-field threshold for Farley Buneman instability somewhat, increases the upper altitude limit, and turns the waves.

[47] To understand how Farley Buneman waves behave quantitatively in a realistic ionosphere, wave heating, cooling, and vertical transport must be considered nonlocally and self consistently. *Michhue* [2010] developed a one-dimensional hybrid kinetic/fluid theory for this problem expected to be accurate for convection electric fields up to about 75 mV/m. At the center of the theory was a dispersion relation for Farley Buneman waves based on kinetic ions and fluid electrons which included the effects of frictional heating and cooling by inelastic collisions. The electron and ion ratios of specific heat were not imposed but rather emerged from the model equations self consistently. Given a specified convection electric field, the dispersion relation predicted the RMS magnetic aspect angle width and the wave phase speed consistent with the marginal growth condition. Applying the Milikh and Dimant ansatz then yielded a heating rate due to the wave electric fields. The heating rate profile was used to drive a generalized, steady state vertical heat transport model [e.g. *Rees*, 1989; *Schunk and Nagy*, 2000]. From this came estimates of the electron temperature profile, which went back into the Farley Buneman dispersion relation. Iteration to convergence produced estimated wave amplitude and phase speed profiles internally consistent with the specified convection speed and electron temperature profile. The results of the model study were found to be in reasonable agreement with the empirical formulas relating the convection electric field and the Farley Buneman wave Doppler shifts found experimentally.

[48] While progress has been made in understanding Farley Buneman waves, understanding falls short of what would be required to parameterize their effects in general circulation models or to interpret or invert diagnostic information from coherent scatter radars operationally. The various theories and models outlined above are incomplete, rest upon numerous assumptions, and neglect a number of crucial aspects of the auroral ionosphere. Some of the most important shortcomings are addressed below.

3.1. Wave Amplitudes

[49] The first pillar of the Milikh and Dimant ansatz is that the Farley Buneman wave electric fields are comparable in amplitude to the background convection electric field. This was asserted on the grounds of expedience rather than experimental evidence. Remarkably, the *Oppenheim et al.* [2008] and *Dimant and Oppenheim* [2008] numerical simulations seem to support this assumption. However, summarizing the results from a number of auroral sounding rocket experiments, *Bahcivan and Cosgrove* [2010] point out that the relative amplitudes of the published AC electric field perturbations in the auroral *E* region seem to be significantly less than the corresponding background (DC) field amplitudes in nature. *Pfaff* [1995] and the references therein have pointed out that electric field probes artificially underestimate the amplitude of waves with wavelengths less than about twice the boom length. However, another possible interpretation was advanced by *Bahcivan and Cosgrove* [2010], who proposed that the finite vertical background density gradient scale length in the auroral ionosphere essentially modifies the dispersion relation for Farley Buneman waves such that long wavelengths (tens of meters) are significant and that finite parallel wave numbers are preferred. Such waves would be more efficient heat sources than waves in a homogeneous background ionosphere, requiring smaller transverse electric fields to have the same effect on the electron temperature profile.

3.2. Magnetic Aspect Width

[50] The heating rate in a plasma can be expressed in phasor notation as

$$Q = 2\mathbf{E}^* \cdot \sigma^H \cdot \mathbf{E}$$

where the electric field term contains both the background electric field and the wavefield and where σ^H is the Hermitian part of the conductivity tensor. Joule heating is that part of Q due entirely to the background DC electric field, and wave heating is the remainder. Because of the anisotropy of σ, wavefield components parallel to the magnetic field can easily dominate heating.

[51] The second pillar of the Milikh and Dimant ansatz is that the RMS magnetic aspect width, the RMS ratio of $k_\parallel/k_\perp$ for the collection of Farley Buneman waves contributing to the wave turbulence, grows as large as necessary to satisfy the condition for marginal stability. Saturation is by two mechanisms: increasing the RMS aspect width of the irregularities both reduces their linear growth rate directly and also heats the electrons, increasing the ion acoustic speed and the diffusivity and decreasing the growth rate indirectly. The aspect width of the irregularities is therefore crucial to the amount of heating that ultimately takes place.

[52] In the *Oppenheim et al.* [2008] and *Dimant and Oppenheim* [2008] simulations, both transverse and parallel electric fields contribute to wave heating significantly. Under the Milikh and Dimant ansatz, wave heating is entirely by parallel wave electric fields. According to *Bahcivan and Cosgrove* [2010], wave heating by parallel electric fields is greater still, being enhanced by large secular parallel wave numbers inherent in Farley Buneman waves in an *E* region with finite thickness. Discerning between these theoretical perspectives will be essential for understanding and parameterizing wave heating during auroral activity.

3.3. Ion Acoustic Speed

[53] A continuing source of confusion and controversy in this discipline arises from the definition of the ion acoustic speed, which is central to the theory of modified two-stream waves. Formally, the ion acoustic speed is

$$C_s \equiv \sqrt{\frac{\gamma_e K_b T_e + \gamma_i K_b T_i}{m_i}}$$

where γ_j and T_j refer to the ratio of specific heats and the temperature of species j, respectively, and K_b is Boltzmann's constant. As mentioned above, various studies have found that the Doppler shifts of coherent scatter from the radio aurora either are or are not governed by this characteristic speed (see *Makarevich* [2009] for a recent review of the literature). Assessing the role of the ion acoustic speed experimentally is challenging, however, because of its variability.

[54] Another source of confusion are the ratios of specific heats, which are not unity in the context of waves in the auroral *E* region. *Farley and Providakes* [1989] argue that the ions taking part in Farley Buneman waves should be adiabatic ($\gamma_i = 5/3$) while the electrons should be isothermal with one degree of freedom ($\gamma_e = 3$). The *Oppenheim et al.* [2008] and *Dimant and Oppenheim* [2008] simulations essentially support this, as does the *Michhue* [2010] model at low convection speeds. On the basis of calculations appropriate for the equatorial electrojet, *Hysell et al.* [2007] argued that the ratios of specific heat are functions of altitude and wavelength and that radars with different scattering wavelengths should get different results. Under strong convection, the electrons are expected to develop suprathermal tails, and the fluidic concept of ion acoustic speed loses meaning.

3.4. Neutral Winds

[55] The analysis to this point has neglected provisions for the neutral winds. During the event considered here, the lower thermospheric winds were constant, nearly transverse to the radar lines of sight, and presumed to have had little effect on the coherent scatter data, although we cannot assume this with great conviction in the absence of measured wind profiles. Generally, we know that the winds in the auroral lower thermosphere are frequently structured and dynamic, characterized by strong shears and narrow jets. In the case of the JOULE II experiment, wind speeds were as large as about 175 m/s, and shears as large as about 30 m/s/km.

[56] Statements regarding the ion acoustic speed above should be reinterpreted as the ion acoustic speed in the ion frame of reference. This frame is shifted by the horizontal wind speed in the lower *E* region. We should therefore expect to have to correct for all phase velocity measurements, in situ and ground based, for the horizontal wind velocity. In the event described above, FPI observations suggested that the neutral winds in the lower thermosphere were directed nearly transverse to the radar line of sight. This is a rough approximation at best, since a broad range of radar azimuths was considered and since the winds in the lower thermosphere typically vary in magnitude and direction considerably with height.

3.5. Altitude-Dependent Collisions

[57] Linear theory predicts that the amount by which the convection electric field must exceed the ion acoustic speed for wave onset depends on the electron- and ion-neutral collision frequencies, increasing with decreasing altitude. Waves are expected to emerge first at altitudes concentrated where the threshold convection electric field has a minimum, which was near 110 km altitude in the model studies of *Michhue* [2010]. At these altitudes, the effects of collisions on threshold should be small. However, the temperature profiles used for those studies were based on quiet time climatology. Joule and particle heating can modify the temperature profiles in such a way as to decrease the altitude where the threshold electric field has a minimum. The effect would be to increase the threshold for wave onset. This may explain the occasional absence of coherent scatter in places and times when the PFISR showed electric fields stronger than about 20 mV/m, although absorption likely played a role as well. Furthermore, even waves concentrated at 110 km will extend downward in altitude, and a nonlocal treatment is warranted to assess the effects of collisions comprehensively.

4. Summary

[58] Radar and optical data from a substorm event on Feb. 19, 2012 have been presented. The emphasis has been on aspects of the radar aurora revealed through VHF radar imaging. We find that *E*-region coherent scatter is generally observed when the convection electric field is above threshold for Farley Buneman instability (about 20 mV/m) except where ionospheric absorption is strong enough to prevent the reception of the radar signals, which necessarily travel along low elevation angles and long paths through the *D* region in order to satisfy the condition for field-aligned backscatter.

[59] For much of the event, the radar backscatter was spatially diffuse (diffuse radar aurora) and separated by latitude into two bands with a discrete auroral arc in between. Discrete arcs sometimes defined either the poleward or the equatorward boundary of the diffuse radar auroral regions. At times, structured regions (in terms of power and spectral characteristics) emerged in the VHF radar data, generally in the vicinity of discrete auroral forms (arcs and torches). That the Doppler shifts of the echoes on opposite sides of discrete auroral arcs and torches generally differed substantially from one side to the other may be evidence of field-aligned current.

[60] Pulse compression, a rapid pulse repetition frequency, and pulse-to-pulse analysis made it possible to sort the

coherent scatter echoes into compact range, Doppler, and time bins with minimal ambiguity. Aperture synthesis radar imaging furthermore made it possible to assign the echoes to compact azimuth angle bins. All together, this facilitated reasonably direct comparisons between the coherent scatter observations and line-of-sight ion drifts measured by the Poker Flat Incoherent Scatter Radar. With the assumption of equipotential magnetic field lines, the F region ISR data could be mapped into the E region and compared with estimates of the convection derived from the coherent scatter using empirical formulas found in earlier studies. Overall, the convection velocity estimates derived from the radar aurora appear to be reasonably accurate and can be used, for example, to develop regional maps of the convection pattern.

[61] Numerical simulations presented by *Oppenheim et al.* [2008] and *Dimant and Oppenheim* [2008] give a basis for understanding the aforementioned empirical relationships. However, these simulations were conducted in compact volumes and did not consider altitude variations in the plasma and neutral state parameters, nonlocal effects arising from these variations, long-range transport along magnetic field lines, photochemical changes, or the possible interactions between small-scale Farley Buneman waves and other, large-scale waves like gradient drift waves. Expanding the particle in cell codes to encompass these phenomena is still prohibitively expensive computationally. A hybrid computational approach, capable of capturing kinetic effects in Farley Buneman waves together with effects at intermediate scales, is necessary to quantify the behavior of the radio aurora and to unlock its diagnostic potential.

References

Aster, R. C., B. Borchers, and C. H. Thurber (2005), *Parameter Estimation and Inverse Problems*, Elsevier, New York.

Bahcivan, H. (2007), Plasma wave heating during extreme electric fields in the high-latitude E region, *Geophys. Res. Lett.*, *34*, L15106, doi:10.1029/2006GL029236.

Bahcivan, H., and R. Cosgrove (2010), On the generation of large wave parallel electric fields responsible for electron heating in the high-latitude E region, *J. Geophys. Res.*, *115*, A10304, doi:10.1029/2010JA015424.

Bahcivan, H., D. L. Hysell, M. F. Larsen, and R. F. Pfaff (2005), 30 MHz imaging radar observations of auroral irregularities during the JOULE campaign, *J. Geophys. Res.*, *110*, A05307, doi:10.1029/2004JA010975.

Bahcivan, H., D. L. Hysell, D. Lummerzheim, M. F. Larsen, and R. F. Pfaff (2006), Observations of collocated optical and radar auroras, *J. Geophys. Res.*, *111*, A12308, doi:10.1029/2006JA011923.

Buneman, O. (1963), Excitation of field aligned sound waves by electron streams, *Phys. Rev. Lett.*, *10*, 285–287.

Dimant, Y. S., and M. M. Oppenheim (2004), Ion thermal effects on E-region instabilities: Linear theory, *J. Atmos. Sol. Terr. Phys.*, *66*, 1639–1654.

Dimant, Y. S., and M. M. Oppenheim (2008), Large-scale 2D and 3D simulations of plasma turbulence in the lower ionosphere, paper presented at 50th Annual Meeting of the Division of Plasma Physics, Am. Phys. Soc., Dallas, Tex.

Farley, D. T. (1959), A theory of electrostatic fields in a horizontally stratified ionosphere subject to a vertical magnetic field, *J. Geophys. Res.*, *64*, 1225–1233.

Farley, D. T. (1963), A plasma instability resulting in field-aligned irregularities in the ionosphere, *J. Geophys. Res.*, *68*, 6083–6097.

Farley, D. T., and J. F. Providakes (1989), The variation with T_e and T_i of the velocity of unstable ionospheric two-stream waves, *J. Geophys. Res.*, *94*, 15,415–15,420.

Fuller-Rowell, T. J., M. V. Codrescu, R. J. Moffett, and S. Quegan (1994), Response of the Thermosphere and Ionosphere to Geomagnetic Storms, *J. Geophys. Res.*, *99*, 3893–3914.

Greenwald, R. A., W. L. Ecklund, and B. B. Balsley (1973), Auroral currents, irregularities, and luminosity, *J. Geophys. Res.*, *78*, 8193–8203.

Hamza, A. M., and J. P. St-Maurice (1993), A turbulent theoretical framework for the study of current-driven E region irregularities at high latitudes: Basic derivations and application to gradient-free situations, *J. Geophys. Res.*, *98*, 11,587–11,599.

Heinselman, C. J., and M. J. Nicolls (2008), A Bayesian approach to electric field and E-region neutral wind estimation with the Poker Flat Advanced Modular Incoherent Scatter Radar, *Radio Sci.*, *43*, RS5013, doi:10.1029/2007RS003805.

Hysell, D. L., and J. L. Chau (2006), Optimal aperture synthesis radar imaging, *Radio Sci.*, *41*, RS2003, doi:10.1029/2005RS003383.

Hysell, D. L., and J. Drexler (2006), Polarization of E region plasma irregularities, *Radio Sci.*, *41*, RS4015, doi:10.1029/2005RS003424.

Hysell, D. L., J. Drexler, E. B. Shume, J. L. Chau, D. E. Scipion, M. Vlasov, R. Cuevas, and C. Heinselman (2007), Combined radar observations of equatorial electrojet irregularities at Jicamarca, *Ann. Geophys.*, *25*, 457–473.

Hysell, D. L., G. Michhue, M. F. Larsen, R. Pfaff, M. Nicolls, C. Heinselman, and H. Bahcivan (2008), Imaging radar observations of Farley Buneman waves during the JOULE II experiment, *Ann. Geophys.*, *26*, 1837–1850.

Hysell, D. L., G. Michhue, M. J. Nicolls, C. J. Heinselman, and M. F. Larsen (2009), Assessing auroral electric field variance with coherent and incoherent scatter radar, *J. Atmos. Sol. Terr. Phys.*, *71*, 697–707.

Hysell, D. L., H. C. Aveiro, and J. L. Chau (2012), Ionospheric irregularities: Frontiers, in *Modeling the Ionosphere-Thermosphere System*, *Geophys. Monogr. Ser.*, doi:10.1029/2012GM001226, in press.

Kagan, L. M., and M. C. Kelley (2000), A thermal mechanism for generation of small-scale irregularities in the ionospheric E-region, *J. Geophys. Res.*, *105*, 5291–5303.

Makarevich, R. A. (2009), Coherent radar measurements of the Doppler velocity in the auroral E region, *Radio Sci. Bull.*, *32*, 33–46.

Michhue, G. P. (2010), Electron heating by Farley Buneman waves at polar latitudes, Master's thesis, Cornell Univ., Ithaca, N. Y.

Milikh, G. M., and Y. S. Dimant (2002), Kinetic model of electron heating by turbulent electric field in the E region, *Geophys. Res. Lett.*, *29*(12), 1575, doi:10.1029/2001GL013935.

Milikh, G. M., and Y. S. Dimant (2003), Model of anomalous electron heating in the E region: 2. Detailed numerical modeling, *J. Geophys. Res.*, *108*(A9), 1351, doi:10.1029/2002JA009527.

Nielsen, E., and K. Schlegel (1983), A first comparison of STARE and EISCAT electron drift velocity measurements, *J. Geophys. Res.*, *88*, 5745–5750.

Nielsen, E., and K. Schlegel (1985), Coherent radar Doppler measurements and their relationship to the ionospheric electron drift velocity, *J. Geophys. Res.*, *90*, 3498–3504.

Oppenheim, M. M., and Y. S. Dimant (2004), Ion thermal effects on E-region instabilities: 2-D kinetic simulations, *J. Atmos. Sol. Terr. Phys.*, *66*, 1655–1668.

Oppenheim, M. M., Y. Dimant, and L. Dyrud (2008), Large scale simulations of 2D fully kinetic Farley Buneman turbulence, *Ann. Geophys.*, *26*, 543–553.

Pfaff, R. F. (1995), Comparison of wave electric field measurements of two-stream instabilities in the auroral and equatorial electrojets, in *Plasma Instabilities in the Ionospheric E-Region: Proceedings of a Workshop Held at the Max-Planck-Institut für Aeronomie in Katlenburg-Lindau, Germany, 24–26 October, 1995*, edited by K. Schlegel, pp. 19–22, Cuvillier, Göttingen, Germany.

Providakes, J. F., D. T. Farley, W. E. Swartz, and D. Riggin (1985), Plasma irregularities associated with a morning discrete auroral arc: Radar interferometer observations and theory, *J. Geophys. Res.*, *90*, 7513–7523.

Rees, M. H. (1989), *Physics and Chemistry of the Upper Atmosphere*, Cambridge Univ. Press, New York.

Schlegel, K., and J. P. St.-Maurice (1981), Anomalous heating of the polar E region by unstable plasma waves: 1. Observations, *J. Geophys. Res.*, *86*, 1447–1452.

Schunk, R. W., and A. F. Nagy (2000), *Ionospheres: Physics, Plasma Physics, and Chemistry*, Cambridge Univ. Press, Cambridge, U. K.

St.-Maurice, J. P. (1990), Electron heating by plasma waves in the high-latitude E region ionosphere and related effects: Theory, *Adv. Space Res.*, *10*, 239–249.

St.-Maurice, J. P., and R. S. Kissack (2000), The role played by thermal feedback in heated Farley-Buneman waves at high latitudes, *Ann. Geophys.*, *18*, 532–546.

St.-Maurice, J.-P., and R. Laher (1985), Are observed broadband plasma wave amplitudes large enough to explain the enhanced electron temperatures of the high-latitude E region?, *J. Geophys. Res.*, *90*, 2843–2850.

St.-Maurice, J. P., K. Schlegel, and P. M. Banks (1981), Anomalous heating of the polar E region by unstable plasma waves: 2. Theory, *J. Geophys. Res.*, *86*, 1453–1462.

Tsunoda, R. T., R. I. Presnell, and R. L. Leadabrand (1974), Radar auroral echo characteristics as seen by a 398 MHz phased array radar operated at Homer, Alaska, *J. Geophys. Res.*, *79*, 4709–4724.

Tsunoda, R. T., R. I. Presnell, Y. Kamide, and S. I. Akasofu (1976), Relationship of radar aurora, visual aurora, and auroral electrojets in the evening sector, *J. Geophys. Res.*, *81*, 6005–6015.

Woodman, R. F., and J. L. Chau (2002), First Jicamarca radar observations of two-stream E region irregularities under daytime counter equatorial electrojet conditions, *J. Geophys. Res.*, *107*(A12), 1482, doi:10.1029/2002JA009362.